Protein analysis by Mach-Zehnder interferometers with a hybrid plasmonic waveguide with nano-slots

CHEN CHEN, XUN HOU, AND JINHAI SI*

Key Laboratory for Physical Electronics and Devices of the Ministry of Education and Shaanxi Key Lab of Information Photonic Technique, School of Electronics and Information Engineering, Xi'an Jiaotong University, Xi'an 710049, China

jinhaisi@mail.xjtu.edu.cn

Abstract: Optical biosensing devices for the affinity analysis of molecular binding events could offer significant advantages over current analytical methods. However, most of those excited with a single optical mode are "blind" to the conformational change of bound molecules. We succeeded in designing Mach-Zehnder interferometers (MZI) with a hybrid plasmonic (HP) waveguide with nano-slots. By addressing the structure with dual polarizations, the optogeometrical properties (density and thickness) of protein layers have been determined without ambiguity. Differences in the hybrid mode dispersion between the transverse electric (TE) and transverse magnetic (TM) modes separately allow the determination of the thickness and the density at all stages during the molecular interaction. Moreover, nano-slots can be equated with an effective optical capacitance resulting in strong field confinement and low propagation loss. A proof of concept is conducted by analyzing the conformational change of HepV, a recombinant fragment of collagen V, during complicated molecular interaction. Instead of wavelength interrogation, a cost-effective method with output intensity variation at particular wavelengths due to "resonance phenomena" was employed to monitor the biological event.

OCIS codes: (130.3120) Integrated optics devices; (130.6010) Sensors; (230.7370) Waveguides.

References and links

1. D. Nelson and M. Cox, *Lehninger Principles of Biochemistry* (W.H. Freeman and Company 2005).
2. S. R. Hammes, "The further redefining of steroid-mediated signaling," Proc. Natl. Acad. Sci. U.S.A. **100**(5), 2168–2170 (2003).
3. A. Warshel, P. K. Sharma, M. Kato, Y. Xiang, H. Liu, and M. H. Olsson, "Electrostatic Basis for Enzyme Catalysis," Chem. Rev. **106**(8), 3210–3235 (2006).
4. M. A. Cooper, "Optical biosensors in drug discovery," Nat. Rev. Drug Discov. **1**(7), 515–528 (2002).
5. F. Ye, *Label-Free Biosensor Methods in Drug Discovery* (Springer, 2015)
6. K. E. Coan, M. J. Swann, and J. Ottl, "Measurement and Differentiation of Ligand-Induced Calmodulin Conformations by Dual Polarization Interferometry," Anal. Chem. **84**(3), 1586–1591 (2012).
7. F. Dell'Olio, D. Conteduca, C. Ciminelli, and M. N. Armenise, "New ultrasensitive resonant photonic platform for label-free biosensing," Opt. Express **23**(22), 28593–28604 (2015).
8. B. Drapp, J. Piehler, A. Brecht, G. Gauglitz, B.J. Luff, and J. Ingenhoff, "Integrated optical Mach-Zehnder interfrometers as simazine imuunoprobes," Sens. Act. B **39**(1–3), 277–282 (1997).
9. M. Kitsara, K. Misiakos, I. Raptis, and E. Makarona, "Integrated optical frequency-resolved Mach-Zehnder interferometers for label-free affinity sensing," Opt. Express **18**(8), 8193–8206 (2010).
10. B. J. Luff, S. James Wilkinson, J. Piehler, U. Hollenbach, J. Ingenhoff, and N. Fabricius, "Integrated Optical Mach–Zehnder Biosensor," J. Lightwave Technol. **16**(4), 583–592 (1998).
11. B. Y. Shew, C. H. Kou, Y. C. Huang, and Y. H. Tsai, "UV-LIGA interferometer biosensor based on the SU-8 optical waveguide," Sens. Act. A **120**(2), 383–389 (2005).
12. F. Prieto, B. Sepulveda, A. Calle, A. Llobera, C. Dominguez, A. Abad, A. Montoya, and L.M. Lechuga, "An integrated optical interferometric nanodevice based on silicon technology for biosensor applications," Nanotechnology **14**(8), 907–912 (2003).
13. W. C. Tsai and I. C. Li, "SPR-based immunosensor for determining staphylococcal enterotoxin A," Sens. Act. B **136**(1), 8–12 (2009).
14. A. I. Lao, X. Su, and K. M. Aung, "SPR study of DNA hybridization with DNA and PNA probes under stringent conditions," Biosens. Bioelectron. **24**(6), 1717–1722 (2009).

15. L. Xu, V. G. Vaidyanathan, and B. P. Cho, "Real-time surface plasmon resonance study of biomolecular interactions between polymerase and bulky mutagenic DNA lesions," Chem. Res. Toxicol. **27**(10), 1796–1807 (2014).

16. R. C. Jorgenson and S. S. Yee, "A fiber-optic chemical sensor based on surface plasmon resonance," Sens. Act. B **12**(3), 213–220 (1993).

17. P. Kozma, F. Kehl, E. Ehrentreich-Förster, C. Stamm, and F. F. Bier, "Integrated planar optical waveguide interferometer biosensors: A comparative review," Biosens. Bioelectron. **58**(58), 287–307 (2014).

18. M. C. Estevez, M. Alvarez, and M. L. Lechuga, "Integrated optical devices for lab-on-a-chip biosensing applications," Laser Photonics Rev. **6**(4), 463–487 (2012).

19. R. Méjard, H. J. Griesser, and B. Thierry, "Optical biosensing for label-free cellular studies," Trends Analyt. Chem. **53**, 178–186 (2014).

20. J. N. Anker, W. P. Hall, O. Lyandres, N. C. Shah, J. Zhao, and R. P. Van Duyne, "Biosensing with plasmonic nanosensors," Nat. Mater. **7**(6), 442–453 (2008).

21. Q. Wang, R. Liu, X. Yang, K. Wang, J. Zhu, L. He, and Q. Li, "Surface plasmon resonance biosensor for enzyme-free amplified microRNA detection based on gold nanoparticles and DNA supersandwich," Sens. Act. B **223**, 613–620 (2016).

22. F. Dell'Olio, D. Conteduca, M. De Palo, and C. Ciminelli, "Design of a New Ultracompact Resonant Plasmonic Multi-Analyte Label-Free Biosensing Platform," Sensors (Basel) **17**(8), 1810 (2017).

23. A. Bozzola, S. Perotto, and F. De Angelis, "Hybrid plasmonic-photonic whispering gallery mode resonators for sensing: a critical review," Analyst (Lond.) **142**(6), 883–898 (2017).

24. X. Kong, E. Li, K. Squire, Y. Liu, B. Wu, L. J. Cheng, and A. X. Wang, "Plasmonic nanoparticles-decorated diatomite biosilica: extending the horizon of on-chip chromatography and label-free biosensing," J. Biophotonics **10**(11), 1473–1484 (2017).

25. M. Malmqvist, "Biospecific interaction analysis using biosensor technology," Nature **361**(6408), 186–187 (1993).

26. G. H. Cross, A. A. Reeves, S. Brand, J. F. Popplewell, L. L. Peel, M. J. Swann, and N. J. Freeman, "A new quantitative optical biosensor for protein characterisation," Biosens. Bioelectron. **19**(4), 383–390 (2003).

27. M. J. Swann, L. L. Peel, S. Carrington, and N. J. Freeman, "Dual-polarization interferometry: an analytical technique to measure changes in protein structure in real time, to determine the stoichiometry of binding events, and to differentiate between specific and nonspecific interactions," Anal. Biochem. **329**(2), 190–198 (2004).

28. H. Berney and K. Oliver, "Dual polarization interferometry size and density characterisation of DNA immobilisation and hybridisation," Biosens. Bioelectron. **21**(4), 618–626 (2005).

29. G. H. Cross, A. Reeves, S. Brand, M. J. Swann, L. L. Peel, N. J. Freeman, and J. R. Lu, "The metrics of surface adsorbed small molecules on the Young's fringe dual-slab waveguide interferom," J. Phys. D Appl. Phys. **37**(1), 74–80 (2004).

30. D. Conteduca, F. Dell'Olio, F. Innone, C. Ciminelli, and M. N. Armenise, "Rigorous design of an ultra-high Q/V photonic/plasmonic cavity to be used in biosensing applications," Opt. Laser Technol. **77**, 151–161 (2016).

31. N. Liu, M. L. Tang, M. Hentschel, H. Giessen, and A. P. Alivisatos, "Nanoantenna-enhanced gas sensing in a single tailored nanofocus," Nat. Mater. **10**(8), 631–636 (2011).

32. A. E. Eter, T. Grosjean, P. Viktorovitch, X. Letartre, T. Benyattou, and F. I. Baida, "Huge light-enhancement by coupling a bowtie nano-antenna's plasmonic resonance to a photonic crystal mode," Opt. Express **22**(12), 14464–14472 (2014).

33. J. Zhang, Q. Song, H. Tian, X. Zhang, H. Wu, J. Wang, C. Yu, G. Li, D. Fan, and P. Yuan, "A double-ring Mach–Zehnder interferometer sensor with high sensitivity," J. Phys. D Appl. Phys. **45**(45), 1–5 (2012).

34. R. J. Wenstrup, J. B. Florer, E. W. Brunskill, S. M. Bell, I. Chervoneva, and D. E. Birk, "Type V collagen controls the initiation of Collagen Fibril Assembly," J. Biol. Chem. **279**(51), 53331–53337 (2004).

35. F. Delacoux, A. Fichard, C. Geourjon, R. Garrone, and F. Ruggiero, "Molecular Features of the Collagen V Heparin Binding Site," J. Biol. Chem. **273**(24), 15069–15076 (1998).

36. S. Ricard-Blum, L. L. Peel, F. Ruggiero, and N. J. Freeman, "Dual polarization interferometry characterization of carbohydrate-protein interactions," Anal. Biochem. **352**(2), 252–259 (2006).

37. N. M. Green, "Avidin," Adv. Protein Chem. **29**, 85–133 (1975).

38. R. Lide David *Handbook of Chemistry and Physics* (CRC 2008).

39. CF Bohren and DR Huffman. *Absorption and Scattering of Light by Small Particle* (Wiley 1983)

40. G. Bartal, R. F. Oulton, V. J. Sorger, and X. Zhang, "A Hybrid Plasmonic waveguide for Subwavelength Confinement and Long Range Propagation," Nat. Photonics **2**(8), 496–500 (2008).

41. J. Dostalek, J. Ctyroky, J. Homola, E. Brynda, M. Skalsky, P. Kekvindova, J. Spirkova, J. Skvor, and J. Schrofel, "Surface plasmon resonance biosensor based on integrated optical waveguide," Sens. Act. B **76**(1–3), 8–12 (2001).

42. Y. Gao, Q. Gan, Z. Xin, X. Cheng, and F. J. Bartoli, "Plasmonic Mach-Zehnder interferometer for Ultrasensitive On-Chip Biosensing," ACS Nano **5**(12), 9836–9844 (2011).

43. H. Awrin, "Ellipsometry on thin organic layers of biological interest: characterization and applications," Thin Solid Films **377**, 48–56 (2002).

44. J. Wen and T. Arakawa, "Refractive index of proteins in aqueous sodium chloride," Anal. Biochem. **280**(2), 327–329 (2000).

45. T. M. Davis and W. D. Wilson, "Determination of the refractive index increments of small molecules for correction of surface plasmon resonance data," Anal. Biochem. **284**(2), 348–353 (2000).
46. G. S. Nikolic, M. D. Cakic, and L. A. Ilic, "Specific refractive index increments of insulin," J. Serb. Chem. Soc. **66**(6), 397–401 (2001).
47. J. A. De Feijter, J. Benjamins, and F. A. Veer, "Ellipsometry as a tool to study the adsorption behavior of synthetic and biopolymers at the air–water interface," Biopolymers **17**(7), 1759–1772 (1978).
48. http://www.bellexinternational.com/products/cytop/

1. Introduction

Biomolecules exert their biological effects via binding to other molecules. A significant number of interactions including antibody–antigen [1], receptor–hormone [2] and enzyme–substrate [3] play a crucial role in physiological activities. Thus, precise detection of biomolecules especially proteins is strongly required in the healthcare and pharmaceutics [4,5]. Nuclear Magnetic Resonance (NMR) with isotope-labeled biological sample is common used for determining protein conformation, yet high-quality protein consumption [6]. Without sacrificing the resources for more extensive biophysical characterization, label-free biochemical technologies, particularly evanescent wave biosensor techniques [7–12] provide considerable insight into biological events. Mechanism of most label-free biosensors is based on evanescent field sensing. Within the evanescent field, analytes recognize with partner receptors already immobilized onto the surface of waveguide and thus affecting the guiding properties of waveguide, concretely, shifts in effective mode index. Various configurations have been investigated to convert effective mode index changes, caused by unit changes in biolayer property and bulk refractive index, into detectable power changes, among which the most widely adopted are the integrated Mach–Zehnder Interferometer(MZI) [8–10] and surface plasmon resonance (SPR) techniques [13–16]. Integrated MZI has great advantages on mechanical stability, capability in mass production and miniaturization [17]. Moreover, such device has a broad dynamic range and long interaction length. However, it has inherent drawback originating from its working principle. The evanescent wave decays exponentially with decay length on the order of 0.1-1μm [18], thus it only senses the changes taking place on the surface of waveguide due to higher intensity of evanescent field in this particular region. The shifts in bulk solution is hardly considered, whereas the bulk index has exact influence on the sensor response.

In the latter case, the surface plasmon resonance (SPR) technique has been widely used in the detection of biomolecular interaction [19–21], due to its highly confined optical field at the metallic surface. To overcome the intrinsic bulk of conventional SPR and offer the prospect of lab-on-chip microsystems, technologies based on localized surface plasmon resonance (LSPR) are currently under investigation. Caterina Ciminelli and associates have deigned a novel ultracompact resonant plasmonic platform for multi-analyte detection [22]. The promising platform comprises a number of biosensors, each of which is based on a plasmonic cavity, consisting of periodic metal structure deposited on a silica substrate. Francesco De Angelis *et al.* have reported a single protein sensing in real time using LSPR supported by gold nanorods in a critical review [23]. Alan X. Wang *et al.* firstly proposed that the plasmonic nanoparticle-decorated diatomite biosilica as matrix is capable of separating and detecting small molecules from real biofluid with ultra-high detection sensitivity down to 1ppm [24]. The physics of SPR techniques relies on measurements to single transverse magnetic (TM) polarization [25]. However, due to single measurement, it is unable to simultaneously differentiate shifts in the biolayer thickness a, refractive index of layer Δn_l. Thus, SPR is hardly capable of distinguishing between a thick sparse layer and a thin dense layer. To gain greater information of biological events taking place at these interfaces two measurements are required. Moreover, researchers lay increasing stress on the concept of proteome which can be broadly interpreted as proteins expressed by genome, resulting in an obvious requirement for huge collaborative effort in protein signature [26]. Recently, a dual polarization interferometry (DPI) [27,28] with its ability to monitor conformational change of

molecules has been deployed in the field of protein engineering. This commercially available approach has been demonstrated to provide both adlayer thickness a and refractive index n_l in the biological system. However, this technique lacks multiplexing abilities [18] and suffers from a large footprint [29], setting limits on the development and application as biosensor.

Recently emerged hybrid plasmonic technologies [23,30] have attracted widespread attentions in biosensing for its unprecedented sensitivity to small particles, down to a single molecule level. Amongst these, photonic/plasmonic cavity [30–32] has extra advantages of strong energy confined in a region at nanoscale with low input power. It corresponds to a resonance condition obtained at specific wavelength through efficiently coupling between Bloch mode in the photonic crystal cavity and plasmonic mode in the metal slot [30]. Generally, the physical quantity Q-factor and mode volume V enable to evaluate the performance of photonic/plasmonic cavity. High values of the Q/V ratio correspond to a strong light-matter interaction. It has been demonstrated [30] that the Q/V ratio of such photonic/plasmonic cavity can achieve six orders of magnitude with respect to dielectric cavities. In particular, the photonic/plasmonic cavity is suitable for optical trapping which is a fresh application. Optical trapping is to steadily trap and detect biological nanoparticles, such as proteins and nucleic acid, by means of strong optical forces. Low input power of a few milliwatt can avoid the thermophoresis effect and thus providing stable optical traps. Good performance makes such photonic/plasmonic cavity definitely more attractive for the market.

In this article, we report on the design of hybrid plasmonic(HP) waveguide with nano-slots integrated with MZI. The novel device is consist of two parts: HP waveguide with nano-slots constructed in the sensing arm of MZI and MZI structure. For the HP waveguide, two orthogonal polarizations of incident light are applied to the chip, in turn exciting the fundamental quasi-TE mode and fundamental quasi-TM mode (hereafter this text will be abbreviated as TE mode and TM mode) and the modes interrogate the biolayer by means of evanescent tail. In this way, shifts in adlayer thickness Δa and refractive index Δn_l can be determined independently. Moreover, a metal(Ag) cladding in the structure can provide a combination of plasmonic and photonic modes contributing to sub-wavelength confinement with high sensitivity as well as relative long propagation distance. Subsequently, HP waveguide is constructed in the sensing arm of MZI which can provide parallel-controlled trial and improve the performance of pure HP waveguide. In general, wavelength interrogation accomplished by expensive instrument is applied to the detection. Herein, we find that resonance phenomena occurs at particular wavelength and the intensity amplitudes are markedly different presented in the output spectrum. Since power change detection are more sensitive to a small shift in refractive index of the ambient medium [33]. As an alternative, power change detection at specific wavelength using optic-electric detector can significantly enhance cost efficiency. In order to verify the novel architecture, we quantitatively analyze the carbohydrate-protein interaction in which biotinylated heparin is immobilized to the surface through biotin–streptavidin system subsequently, interacting with HepV, a recombinant fragment of collagen V. Collagen V is a member of the fibril subclass of collagens and it plays crucial role in fibrillogenesis [34,35]. Collagen V specifically interacts with a number of extracellular components through its 300nm long predominant triple helical domain which exhibits different molecular forms in tissue [35]. The major form in most tissues is the heterotrimer [α1(V)]2α2(V) which was previously discovered to interact with heparin depending on glycosaminoglycans chains at physiological salt concentrations [35]. Specifically, the heparin binding region is located within a 12kDa fragment in the triple helical part of the α1(V) chain [35,36]. The recombinant fragment (Ile824 to Pro950), referred as HepV, is sufficient for heparin binding and functions as cell adhesion through a cell surface heparan sulfate proteoglycan [35,36]. Therefore, the binding of HepV to heparin can modulates the interaction between collagen V and heparin sulfate proteoglycan in tissues. D-biotin streptavidin model which has been intensely investigated for decades and is used in immunological protocol is utilized for immobilizing heparin on the surface owing to its high

binding affinity with dissociation constant of $K_d = 10^{-15}$ mol/dm³ [37]. The whole process of HepV-heparin interaction is simulated based on the finite-element-method (FEM).

2. HP waveguide with nano-slots

2.1 Architecture of a HP waveguide

The Schematic of HP waveguide with nano-slots is shown in Fig. 1. Figure 1(a) presents the 3D schematic structure of proposed HP waveguide, consisting of a silicon-on-insulator(SOI) rib and a metal (Ag) cladding. The region between Si core and Ag layer is filled with tested analyte. In this way, double nano-slots are formed at both sides of the Si core as well as another slot embedded on the top of Si core. The cross-section view with the optimized geometric parameters is presented in Fig. 1(b). The widths of Si core and lateral nano-slots are denoted as w_{si} and w_{slot}, respectively. The height of Si ridge and upper nano-slot are defined as h_{si} and h_{slot} respectively. In Fig. 1(c), field profile reveals that present configuration can support TE mode and TM mode simultaneously. Assign the values of geometric parameters: w_{si} equals 550nm, h_{si} equals 320nm, w_{slot} and h_{slot} equal 50nm and 80nm, respectively. Thicknesses of Ag cladding and buffer layers (SiO₂) are set as 3μm so as to neglect the influence of simulation boundaries. In the simulation work, the refractive indices [38] of Si and SiO₂ are set as 3.5046 and 1.447, respectively, at operation wavelength of 1.3μm. The wavelength selection [7] is based on a tradeoff between the absorption loss caused by aqueous solution and the broadband light sources. Water optical absorption is smaller at wavelength of 1.3μm, compared with 1.55μm wavelength common used for operation. The permittivity of silver is achieved through Durde- Sommerfeld model [39]:

$$\varepsilon = \varepsilon_\infty - \frac{\omega_p^2}{\omega^2 + j\omega\gamma} \tag{1}$$

where $\varepsilon_{\infty} = 3.1$, $\omega_p = 140 \times 10^{14} rad / s$, and $\gamma = 0.31 \times 10^{14} \ rad /s$.
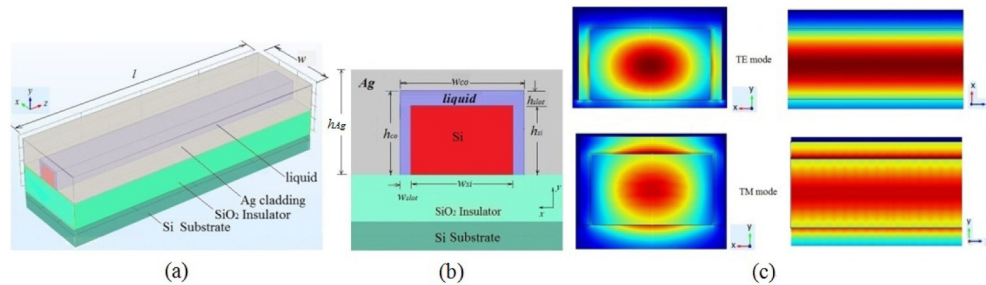

Fig. 1. (a) Schematic of HP waveguide (b) Cross-section view of the DPHP waveguide filled by test liquid. The widths of Si core and lateral slot are denoted as w_{si} and w_{slot}, respectively. The heights of silver cladding, Si core and upper slot are defined as h_{Ag}, h_{si} and h_{slot}, respectively. (c) field profiles of the HP waveguide.

2.2 Theory of a HP waveguide with nano-slots

For most waveguide systems, the evanescent wave decays exponentially with decay length on the order of 0.1-1μm [18], thus it only senses the changes taking place on the surface of waveguide due to higher intensity of evanescent field in this particular region. Therefore, the shifts in bulk solution is hardly considered, whereas the bulk index has exact influence on the sensor response. With regard to the proposed structure, incident light goes through the waveguide and excites surface plasmon in the slots when the phase velocities of the optical mode and that of the surface plasmon match. The field is confined in the slots and sufficiently penetrates into solution. As a result, the bulk refractive index can be measured accurately.

Evidently, the slots are able to store electromagnetic energy resulting in subwavelength optical guiding with low propagation loss. Since the dielectric discontinuity at Si core-solution interface produces a polarization charge [40] which interacts with the plasma oscillations of the metal–solution interface. The gap region can be equated with an effective optical capacitance [40] resulting in strong field confinement and low propagation loss. Since two orthogonal polarizations of incident light are applied to the waveguide, both TE and TM modes propagates inside the silicon rib and the modes interrogate the biolayer by means of evanescent tail. In this way, shifts in adlayer thickness Δa and refractive index Δn_l can be determined independently. Moreover, instead of wavelength interrogation, we take intensity to evaluate the differences in refractive indices including bulk index and biolayer index and thickness. Propagation constant of surface plasmon depends strongly on the wavelength, in comparison with optical modes of traditional dielectric waveguide. Phase-matching condition between an optical mode of dielectric waveguide and a surface plasmon supported by metal (Ag) cladding might be fulfilled only within a narrow spectral band. Therefore, when a broadband light ($1.285\mu m \leq \lambda \leq 1.315\mu m$ in this case) is applied to the waveguide, the spectrum presents a narrow dip with optical energy conversion into surface plasmon [41]. The propagation constant of surface plasmon is extremely sensitive to the shifts in refractive index distribution within evanescent field, thus the position of SPR dip in the spectrum relies on the refractive index of sensed medium. Accordingly, we can explain why transmission varies distinctly only at particular wavelength.

2.3 Model investigation

No doubt, the effective mode index is the essential physical quantity which enables the principle of proposed HP waveguide to be elaborated and understood. The index n_{eff} depends mainly on the waveguide parameters, *i.e.* the dimension of slots (w_{slot} and h_{slot}) and Si core(w_{si} and h_{si}), and biolayer properties including adlayer index n_l and operation wavelength λ. In order to simplify the analysis, we assume water solution with index of 1.33 filled in the nano-slots and the operating wavelength has been always fixed as $1.3\mu m$. With the adopted h_{si} = 320nm and h_{slot} = 80nm, the width of Si core w_{si} and the size of lateral nano-slots w_{slot} influence on effective mode index n_{eff} have been investigated for TE and TM modes (Fig. 2). With w_{slot} remained, a wider Si core produces increasing in the mode index n_{eff} for dual polarizations. Since a large Si core produces stronger guided mode confinement. With w_{si} fixed, the mode index n_{eff} becomes smaller with w_{slot} increasing for TE mode while with a decrease in w_{slot} for TM mode. Lager slots weaken surface plasmon confinement in lateral slots resulting in a decrease in the mode index n_{eff} for TE mode. Meanwhile, energy carried by the vanished surface plasmon is retained in guided mode according to the conservation of energy, probably transferring to surface plasmonic mode in the horizontal slot thus raising the mode index n_{eff} for TM mode. Assuming w_{si} = 550nm and w_{slot} = 50nm, the height of Si core h_{si} and the dimension of upper slot h_{slot} effect on the effective mode index n_{eff} has been studied for dual polarizations as well. With h_{slot} remained, the mode index n_{eff} grows with bulk Si core for both TE and TM modes due to stronger guided mode confinement. With h_{si} remained, a wide gap weakens surface plasmon confined in the upper slot resulting in the mode index n_{eff} reducing for TM mode. Alike, according to energy conservation, the reduced energy ultimately transfers to surface plasmonic mode inside the lateral slots thereby increasing the mode index n_{eff} of TE mode. In addition, propagation loss is considered as a significant parameter for the optimal design. We investigate the propagation loss dependent on the dimension of waveguide core and slots and the results are plotted in Fig. 4 and Fig. 5. We find that the propagation loss achieve the value as low as the order of 10^{-4} in the case that w_{si} = 550nm, h_{si} = 320nm, w_{slot} = 50nm, h_{slot} = 80nm. Therefore, the adopted geometrical dimensions of the proposed DPHP waveguide are selected based on the tradeoff between effective mode index and propagation loss.
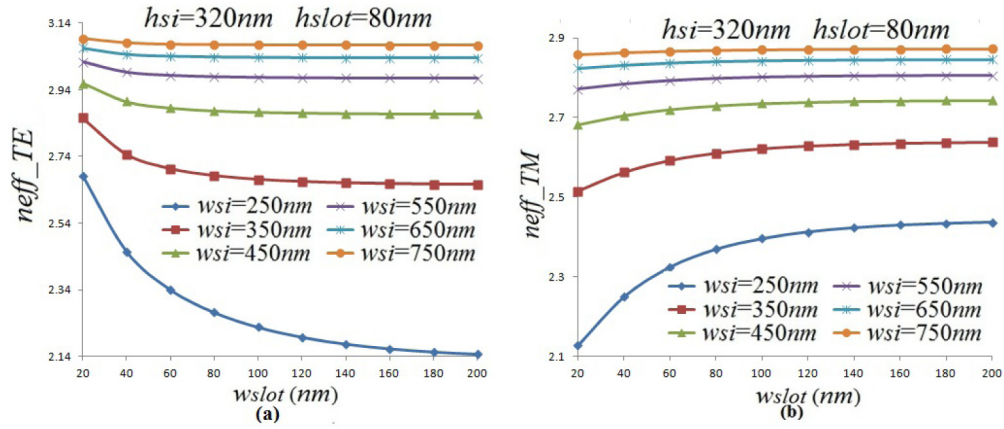
Fig. 2. The effective mode index n_{eff} dependent on the width of Si core w_{si} and the dimension of lateral slots w_{slot}, with adopted h_{si} = 320nm and h_{slot} = 80nm. (a) for TE mode and (b) for TM mode.
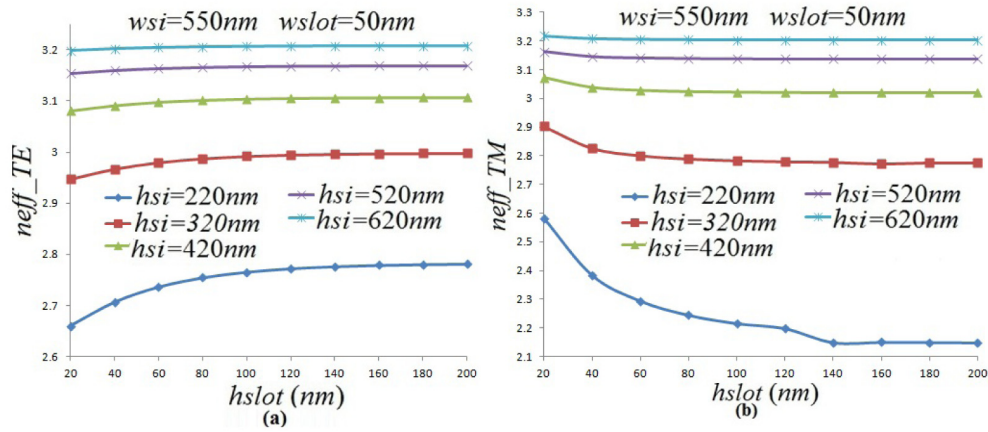

Fig. 3. The effective mode index n_{eff} dependent on the height of Si core h_{si} and the dimension of upper slot h_{slot}, with fixed w_{si} = 550nm and w_{slot} = 50nm. (a) for TE mode and (b) for TM mode.
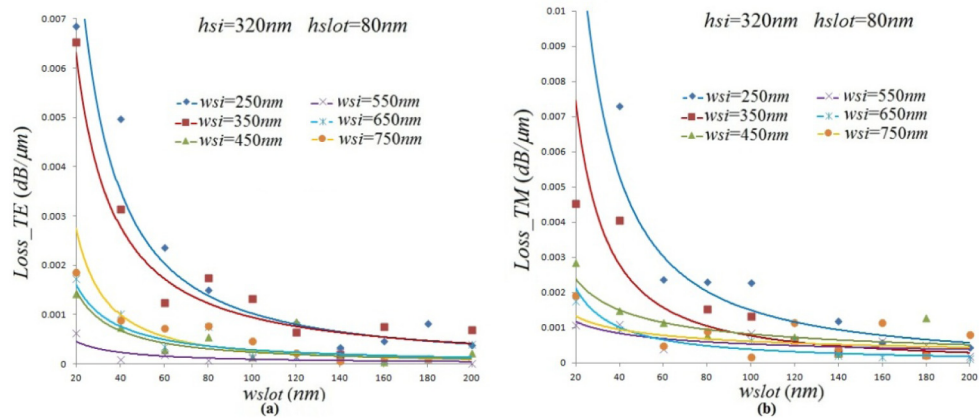

Fig. 4. The width of Si core w_{si} and the dimension of vertical slots w_{slot} influence on the mode propagation loss, with adopted h_{si} = 320nm and h_{slot} = 80nm. (a) for TE mode and (b) for TM mode.
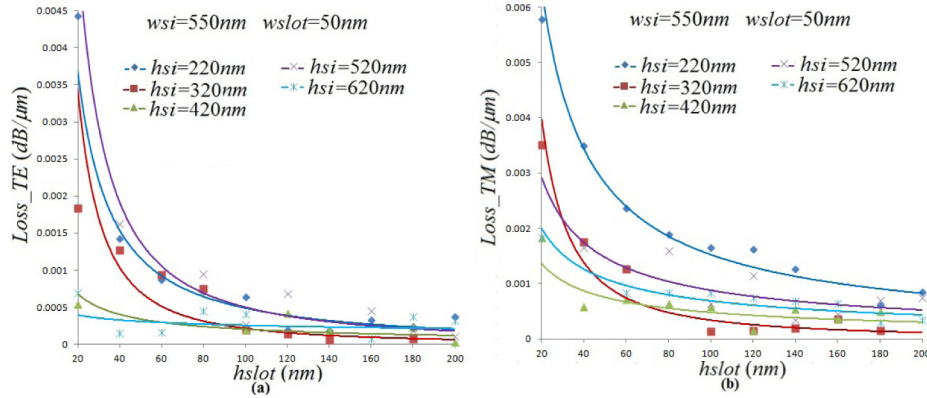
Fig. 5. The height of Si core h_{si} and the dimension of horizontal slot h_{slot} effect on the mode propagation loss, with adopted w_{si} = 550nm and w_{slot} = 50nm. (a) for TE mode and (b) for TM mode.

3. Properties of MZI with a HP waveguide with nano-slots

3.1 Architecture of MZI with a HP waveguide with nano-slots

HP waveguide with nano-slots implemented on the MZI is proposed finally and the model is sketched in Fig. 6. The dimension of device is 71μm in length (L) and 20μm in width (w_L). Sensing and reference arms with identical length L_m = 20μm are separated by the distance D = 11.5μm. The Y-splitter is composed of S-shaped bent wires with bending radius of 19.5μm (r_0 = 19.5μm). The length of HP waveguide l, is 10μm with a width of 6.5μm(w = 6.5μm). From cross-section view of HP waveguide in Fig. 3(c), the geometrical parameters are setting as: w_{si} = 550nm, h_{si} = 320nm, w_{slot} = 50nm, h_{slot} = 80nm and h_{Ag} = 3μm.
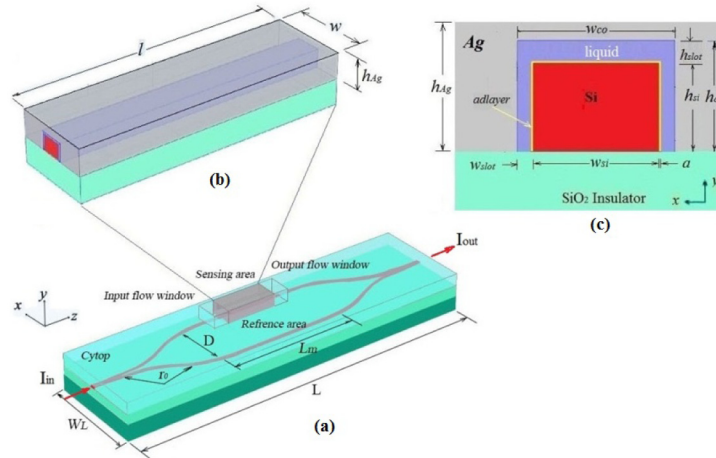

Fig. 6. (a) 3D schematic structure of integrated MZI with 71μm in length (L) and 20μm in width (w_L), with identical length L_m = 20μm in sensing and reference arms and separated by the distance D = 11.5μm, with S-shaped bent wires of bending radius of 19.5μm (r_0 = 19.5μm). (b) the structure of HP waveguide coupled in sensing arm of MZI. Geometrical parameters are set: l = 10μm, w = 6.5μm, w_{si} = 550nm, h_{si} = 320nm, w_{slot} = 50nm, h_{slot} = 80nm and h_{Ag} = 3μm. (c) cross-section view of HP waveguide in sensing area.

Shift in the refractive index within the sensing arm induces a change in the phase velocity between the propagating arms, which is ultimately converted into an intensity modulation at the output of the MZI mathematically expressed as [42]:

$$I_{out} \propto \cos(\Delta\Phi) \tag{2-1}$$

with

$$\Delta\Phi = \frac{2\pi L}{\lambda}(n_{eff\_s\_i} - n_{eff\_r\_i}) \quad (i = TE, TM) \tag{2-2}$$

where I_{out} the output power intensities of the proposed MZI, λ the operating wavelength, L the sensing arm length, $n_{eff\_s\_i}$ (Fig. 8) and $n_{eff\_r\_i}$ (Fig. 9) the effective mode refractive indices of the sensing and reference arms, respectively. For a defined waveguide structure, the $n_{eff\_s\_i}$ is dependent upon operation wavelength as well as biolayer properties while the $n_{eff\_r\_i}$ is only influenced by the wavelength.

3.2 Protein analysis based on an integrated MZI sensor

In order to investigate the integrated MZI capable of monitoring protein conformation herein, HepV-heparin system was emulated based on finite-element-method (FEM) and carried out with COMSOL. Before the measurement, waveguide surface is modified with sulfo-NHS-LC-biotin to provide covalently attached biotin. Generally, HepV-heparin binding event is consist of seven distinct steps [36] which is depicted in Fig. 7: (1) Tris buffer flowing over the biotin functionalized waveguide surface for initial calibration, (2) streptavidin immobilized on the chip surface, (3) initial capture of biotinylated heparin, (4) Tris buffer rinse to remove unbound heparin, (5) second injection of biotinylated heparin over waveguide surface to fully accommodate additional heparin molecules, (6) sodium chloride (NaCl) solution rinse to remove unspecific binding in the process of streptavidin-biotin interaction, (7) introducing recombinant HepV fragment to recognize biotinylated heparin. During the biological event, thickness a and refractive index n_l of adlayer with known numerical values were obtained from typical literature data [36]. Besides, refractive index of buffer solution in each step was calculated according to empirical formula [36] expressed as $n_l = 0.52*(n_p - n_s) + n_s$, where n_p is the refractive index of pure protein (1.465) [43–45] or solvated carbohydrate (1.45) [46]. All data including n_l , n_s and a are presented in the Table 1. The refractive indices (n_{eff_TE} and n_{eff_TM}) were calculated for wavelength spanning 1.285µm ≤ λ ≤ 1.315µm at all stages by finite-element-method (FEM). The fitting curves of the n_{eff_TE} and n_{eff_TM} *versus* the wavelength λ are plotted in Fig. 8. One can see clearly the process of HepV-heparin binding event albeit not in the whole spectrum range. The wavelength interrogation fails to characterize the molecular interaction in this case. Since the spectral resolution of resonance shift detection is less sensitive [33] with regard to a small refractive index change, compared with power change detection. We employ transmission variation at specific wavelengths to interpret the biological event taking place in the sensing arm.
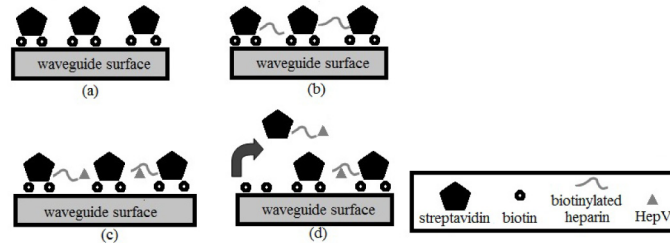

Fig. 7. Schematic representation [30] of the surface structure obtained during the course of the molecular event. (a) streptavidin immobilization. (b) Biotinylated heparin capture. (c) HepV binding with heparin. (d) Loss of streptavidin during injection of HepV.

Table 1. Observed layer characteristics [36] of thickness *a* and refractive index *n_l* during the whole process. Calculated solution refractive index *n_s* in each step by equation *n_l* = 0.52*(*n_p* − *n_s*) + *n_s*.

Material (observation after each step)	Thickness *a* (nm)	RI of layer *n_l*	RI of solution *n_s*
Tris buffer	0	0	1.366
Streptavidin	5.58	1.4037	1.3373
Streptavidin + biotinylated heparin (first injection)	5.46	1.4077	1.3619
Tris buffer rinse	5.48	1.4057	1.3577
Streptavidin + biotinylated heparin (second injection)	5.50	1.4064	1.3592
NaCl rinse	5.38	1.4014	1.3488
HepV binding to heparin	5.33	1.4073	1.3448
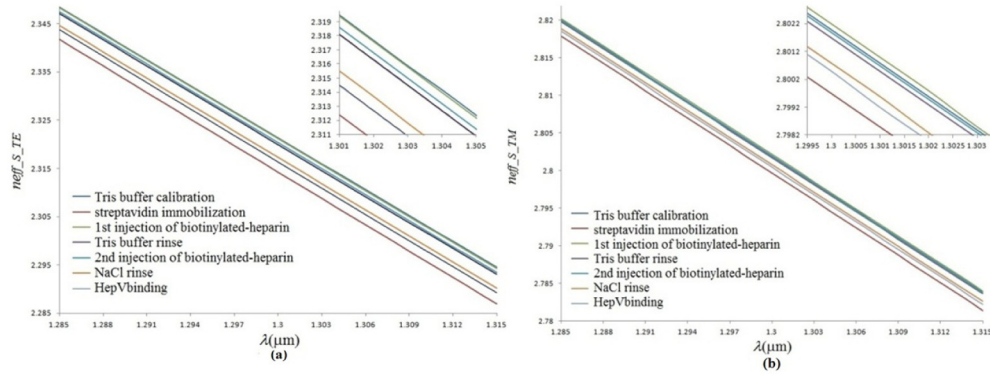
Fig. 8. Simulation results of HepV-heparin binding event at wavelength spanning 1.285µm ≤ λ ≤ 1.315µm for TE mode (a) and TM mode (b) respectively. A plot of wavelength versus effective mode index provides a representation of each step.
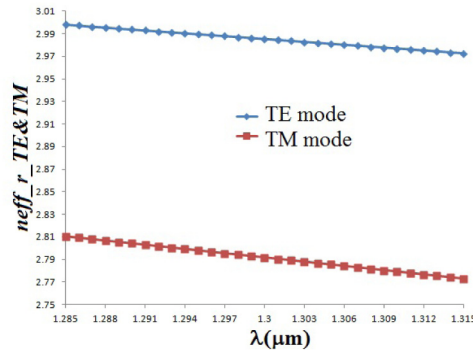

Fig. 9. Simulation results of effective mode refractive indices in reference arm at wavelength spanning 1.285µm ≤ λ ≤ 1.315µm for TE mode (a) and TM mode (b) respectively.

3.3 Property of an integrated MZI sensor

Sensitivities of power change detection, caused by shift in bulk index Δn_s, changes of biolayer index Δn_l and thickness Δa respectively, can be defined as follows:

$$S_{n_{s\_i}} = \frac{\partial T}{\partial n_s} = \frac{\partial T}{\partial \lambda} \cdot \frac{\partial \lambda}{\partial n_{eff\_s\_i}} \frac{\partial n_{eff\_s\_i}}{\partial n_s} \quad (i = TE, TM) \tag{3-1}$$

$$S_{n_l\_i} = \frac{\partial T}{\partial n_l} = \frac{\partial T}{\partial \lambda} \cdot \frac{\partial \lambda}{\partial n_{eff\_s\_i}} \frac{\partial n_{eff\_s\_i}}{\partial n_l} \quad (i = TE, TM) \qquad (3\text{-}2)$$

$$S_{n_l\_i} = \frac{\partial T}{\partial a} = \frac{\partial T}{\partial \lambda} \cdot \frac{\partial \lambda}{\partial n_{eff\_s\_i}} \frac{\partial n_{eff\_s\_i}}{\partial a} \quad (i = TE, TM) \qquad (3\text{-}3)$$

with $\partial T/\partial \lambda$ change rate of output transmission induced by different wavelength. Under this definition, and writing transmission variation $\Delta T(\lambda, n_s, n_l, a)$ in terms of aqueous solution and biolayer parameters:

$$\Delta T(\lambda, n_s, n_l, a)\_i = \frac{\partial T}{\partial n_s} \Delta n_s + \frac{\partial T}{\partial n_l} \Delta n_l + \frac{\partial T}{\partial a} \Delta a \quad (i = TE, TM) \qquad (4)$$

Combining the above equations yields:

$$\Delta T(\lambda, n_s, n_l, a)\_i = \frac{\partial T}{\partial \lambda} \cdot \frac{\partial \lambda}{\partial n_{eff\_s\_i}} \Delta n_{eff\_s\_i} \quad (i = TE, TM) \qquad (5\text{-}1)$$

defining

$$\Delta n_{eff\_s\_i} = \left(\frac{\partial n_{eff\_s\_i}}{\partial n_s} \Delta n_s + \frac{\partial n_{eff\_s\_i}}{\partial n_l} \Delta n_l + \frac{\partial n_{eff\_s\_i}}{\partial a} \Delta a \right) \quad (i = TE, TM) \qquad (5\text{-}2)$$

From Eq. (2), the first-order derivative of transmission with respect to the wavelength is:

$$\frac{\partial T}{\partial \lambda} \propto -\sin(\Delta \Phi) \frac{\partial \Delta}{\partial \lambda} \qquad (6)$$

where

$$\frac{\partial \Delta \Phi}{\partial \lambda} = 2\pi L \frac{\partial}{\partial \lambda} \left(\frac{n_{eff\_s\_i} - n_{eff\_r\_i}}{\lambda} \right) \quad (i = TE, TM) \qquad (7)$$

Combining above equations (Eq. (2)-(7)), we can infer that function $\Delta T(\lambda, n_s, n_l, a)$ must exist one or several minimal values, due to the periodic nature of sinusoidal function and phase difference $\Delta \Phi$. Thus, given the value of bulk index, adlayer index and thickness, resonance phenomenon will occur at particular wavelengths. To obtain transmission variation, we firstly get the function of effective mode index on wavelength through numerical fitting technology. Then set the length of sensing area $l = 10\mu m$ and make Eq. (6) to zero. Extreme value on the function $T\lambda$ can be achieved at special wavelengths. A common 'dip' or resonance phenomenon occurred at specific wavelengths arising from optical energy conversion into surface plasmon. To verify the perspective mentioned above, we employ HepV-heparin interaction system and make simulation based on finite element method. The results are presented in Fig. 10. As predicted, resonance appears at special wavelength (e.g. $\lambda = 1.304\mu m$ for TM mode and $\lambda = 1.296\mu m$ and $1.299\mu m$ for TE mode). With the help of transmission variation at particular wavelength, we can extract the property of adlayer thereby characterizing protein conformation in the binding event. Elaborate efforts are made in the next section.
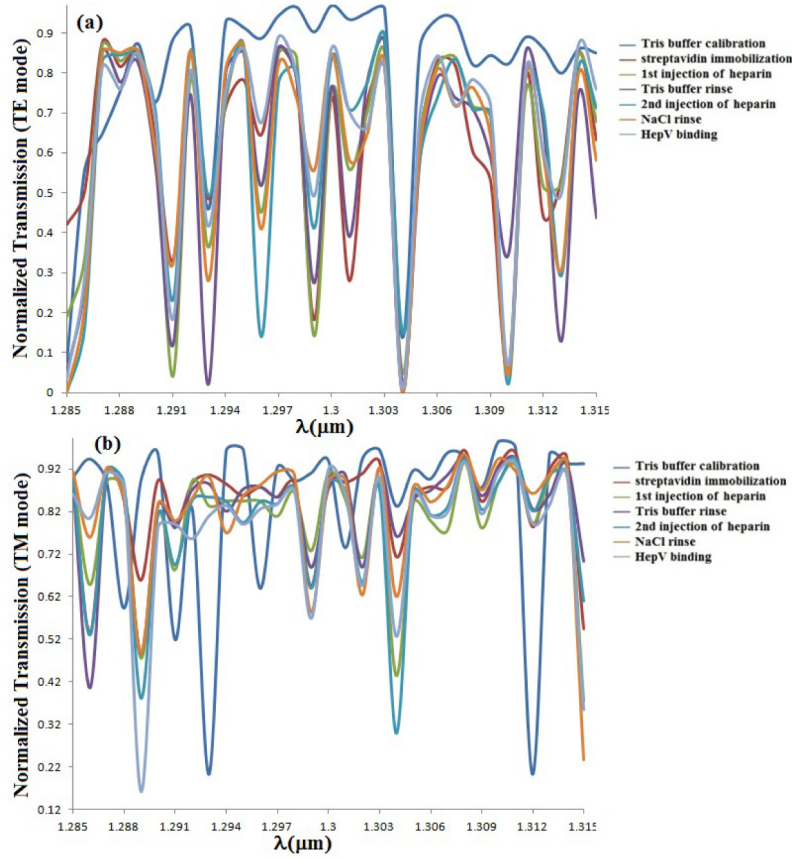
Fig. 10. Output spectrum of Hep V-heparin binding event for TE mode (a). and for TM mode (b).

3.4 Characterization of protein conformation

To extract biolayer thickness and index, we can rewrite Eq. (4) with fixed wavelength as:

$$\begin{bmatrix} \Delta T_{\_TE} \\ \Delta T_{\_TM} \end{bmatrix} = \begin{bmatrix} \dfrac{\partial T_{\_TE}}{\partial n_s} & \dfrac{\partial T_{\_TE}}{\partial n_l} & \dfrac{\partial T_{\_TE}}{\partial a} \\ \dfrac{\partial T_{\_TM}}{\partial n_s} & \dfrac{\partial T_{\_TM}}{\partial n_l} & \dfrac{\partial T_{\_TM}}{\partial a} \end{bmatrix} \begin{bmatrix} \Delta n_s \\ \Delta n_l \\ \Delta a \end{bmatrix} \tag{8}$$

where $\Delta T_{\_i}$ (i = TE, TM) the transmission variation at specific wavelength (herein λ = 1.296μm for TE mode and λ = 1.304μm for TM mode), $\dfrac{\partial T_{\_i}}{\partial n_s}$ transmission shifts caused by bulk index for dual polarizations, $\dfrac{\partial T_{\_i}}{\partial n_l}$ transmission variation due to shifts in adlayer index and $\dfrac{\partial T_{\_i}}{\partial_a}$ shift in adlayer thickness resulting in transmission difference. All the three terms can be obtained by simulation and the data are plotted in Fig. 11, 12 and 13. For the relationship between bulk index and adlayer index in this case, $n_l = 0.52*(n_p - n_s) + n_s$, the expression simplifies to:

$$\begin{bmatrix} \Delta T_{\_TE} \\ \Delta T_{\_TM} \end{bmatrix} = \begin{bmatrix} \dfrac{\partial T_{\_TE^*}}{\partial n_l} & \dfrac{\partial T_{\_TE}}{\partial a} \\ \dfrac{\partial T_{\_TM^*}}{\partial n_l} & \dfrac{\partial T_{\_TM}}{\partial a} \end{bmatrix} \begin{bmatrix} \Delta n_l \\ \Delta a \end{bmatrix} \qquad (9)$$

It is noteworthy that to simplify the numerical calculation, we substitute n_s with n_l via empirical formula [36] $n_l = 0.52*(n_p - n_s) + n_s$, and thus combine $\dfrac{\partial T_{\_TE}}{\partial n_s}$ with $\dfrac{\partial T_{\_TE}}{\partial n_l}$, and $\dfrac{\partial T_{\_TM}}{\partial n_s}$ with $\dfrac{\partial T_{\_TM}}{\partial n_l}$ which subsequently denoted as $\dfrac{\partial T_{\_TE^*}}{\partial n_l}$ and $\dfrac{\partial T_{\_TM^*}}{\partial n_l}$ including both effects of n_s and n_l. The calculated thickness a and refractive index n_l via Eq. (9) share the similar results compared with numerical values measured by DPI [36].
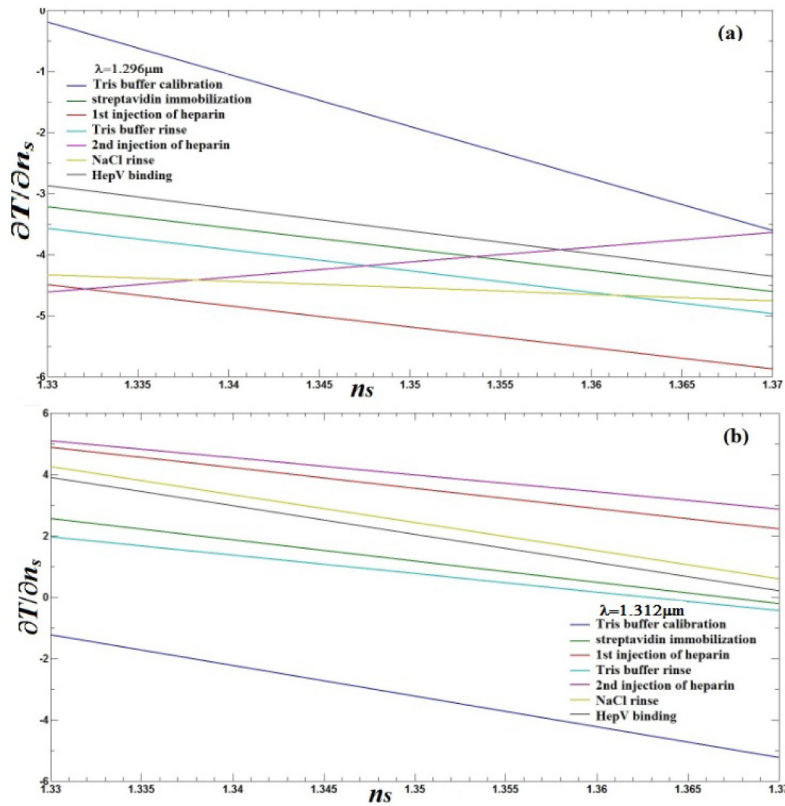

Fig. 11. Partial derivative of the transmission versus bulk index at λ = 1.296μm for TE mode (a) and at λ = 1.312μm for TM mode.

Given the values of thickness and refractive index of biolayer, it is able to calculate the surface mass density during the binding event through De Feijter's formula [47]: $\Gamma = a(n_l - n_s)/(dn/dc)$, with dn/dc the refractive index increment (in $cm^3 \cdot g^{-1}$) which in the case of protein and carbohydrate are 0.186 $cm^3 \cdot g^{-1}$ and 0.142 $cm^3 \cdot g^{-1}$ respectively. The density of adlayer dedicated by streptavidin, biotinylated heparin as well as HepV are 0.357g·cm^{-3}, 0.332 g·cm^{-3} and 0.336 g·cm^{-3} respectively. Integrated with adlayer thickness and density, we can conclude that a thick sparse layer formed after heparin capture and a thin dense layer formed as HepV bound. This phenomenon can be explained that HepV undergoing conformational change on

binding to heparin and a loss of streptavidin Fig. 2(d)) from waveguide surface during HepV injecting thereby a decrease in adlayer thickness and density, compared with streptavidin introduction.
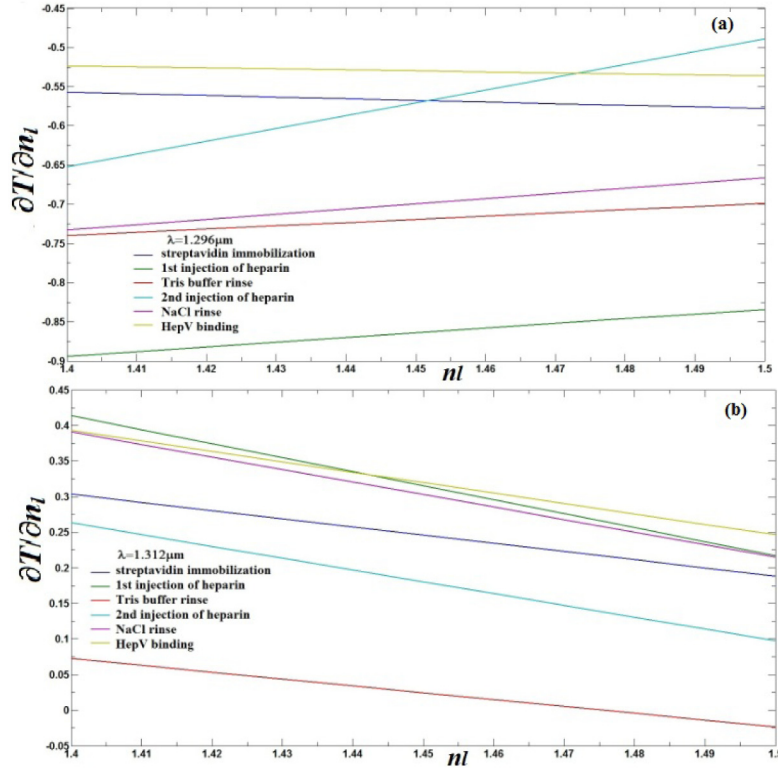

Fig. 12. Partial derivative of the transmission versus adlayer index at λ = 1.296μm for TE mode(a) and at λ = 1.312μm for TM mode.

We have envisaged a CMOS-compatible fabrication process of the designed device. The process can start from a commercial SOI wafer. Alternatively the plasma enhanced chemical vapor deposition (PECVD) technology is used to deposit the SiO_2 and alpha-Si thin film on Si substrate. The photoresist thin film is formed on Si film and the waveguide patterns are constructed using an E-beam lithography so as to gain high resolution. Then an extreme thin aluminum (Al) film with 50nm thickness on the sidewall and 80nm thickness on the top of Si rib was deposited by sputtering process. This step could be followed by the deposition of a metal (Ag) layer with 3μm thickness on the sidewall and top of the Al film by sputtering process. Afterwards, Al film is removed by selectively etched to form the vertical and horizontal slots. The patterned configuration is constructed in the sensing arm of integrated MZI. Reference arm is exposed to the Cytop liquid [48] with refractive index (n≈1.33) similar to water for the control trial. Cytop layer is employed to cover the designed structure so as to avoid external interference. Finally, the sensor is coupled to a microfluidic module in the sensing arm, which allows for sample introduction and real-time monitoring of the binding event.
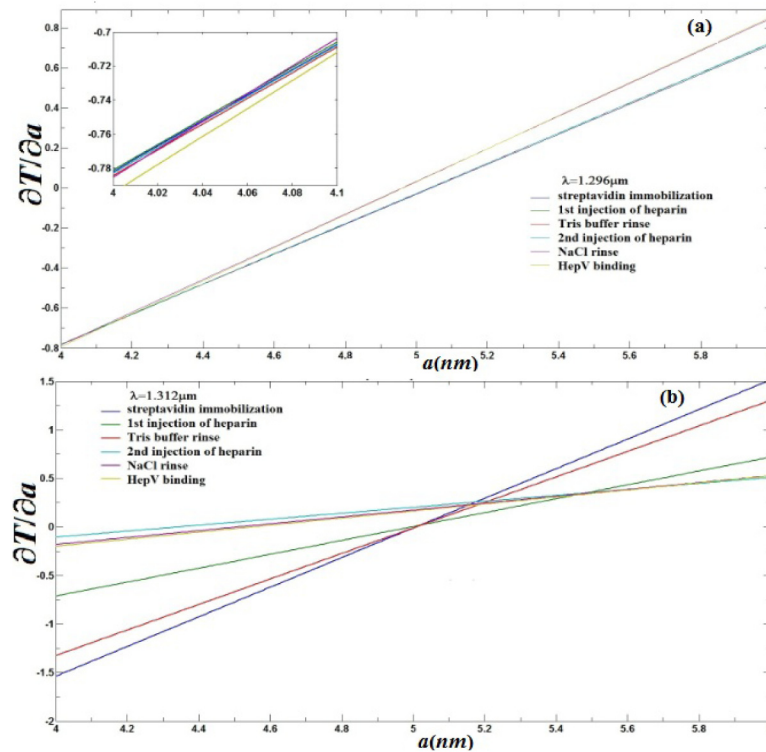
Fig. 13. Partial derivative of the transmission versus adlayer thickness at λ = 1.296mm for TE mode(a) and at λ = 1.312μm for TM mode.

4. Conclusion

We have designed the integrated MZI biosensor and carried out a detailed investigation of modal properties and the performance of the proposed device. The employment of the integrated MZI for protein analysis has been largely discussed. We adopt intensity variation at specific wavelength to interpret the biological event taking place in the sensing arm. Because the intensity change detection can achieve much higher sensitivity in sensing small refractive index change of the ambient medium. In addition, an optic-electric detector can be employed in place of expensive spectrometer thus greatly cutting cost. Biolayer properties can be extracted via Eq. (9) in the text. Given the values of thickness and refractive index of biolayer, it is able to calculate the surface mass density during the binding event. Integrated with adlayer thickness and density, we can characterize the protein conformational change in the molecular interaction that cannot be fulfilled by the current sensors. Therefore, the proposed device is a very potential technique to characterize protein conformation underlying biomolecular interactions. And it lays a good basis for the follow up work. The proposed device used in biochemical sensing experimentally has been planed to carry out.